UNIVERSITY OF CALIFORNIA, IRVINE

A Multimodal Microvascular Imaging System for the Rodent Dorsal Skinfold Window Chamber: Development, Validation and Application

THESIS

submitted in partial satisfaction of the requirements

for the degree of

MASTER OF SCIENCE

in Biomedical Engineering

by

Bita Kianian

Thesis Committee:

Professor Bernard H. Choi, Chair

Associate Professor Elliot Botvinick

Professor Kristen Kelly

2017

TABLE OF CONTENTS:

LIST OF FIGURES III
ACKNOWLEDGEMENTS V
ABSTRACT VI

CHAPTER 1: Background and Significance 1

1.1 Port Wine Stain Birthmarks 1
1.1.1 Current Therapies in The Treatment of Port Wine Stain 2

1.2 Selective Photo-Thermolysis 4

1.3 Angiogenesis and Vasculogenesis After PDL-Treatment 6

CHAPTER 2: Optical imaging 8

2.1 Rodent Dorsal Skinfold Window Chamber Model Selective Photo-Thermolysis 9

2.2 Imaging Modalities 11
2.2.1 Laser speckle Imaging 12

2.2.2 Multispectral/Oxygenation Imaging 17

2.2.2.1 Generation of hemoglobin oxygen saturation maps 20
2.2.3 Fluorescence Imaging 22

2.3 Microvascular Imaging System Walkthrough 23

CHAPTER 3: Validation and Applications: 32

3.1 Long-Term Monitoring of the microvasculature 32

3.2 In-Vitro Flow Phantom Experiment 35

3.3 Results and Discussion 39

CONCLUSION 41
REFERENCES 43
APPENDIX 47

LIST OF FIGURES:

Figure 1: Rodent dorsal skinfold window chamber model 9

Figure 2: Bright field reflectance image and raw speckle image of microvasculature 13

Figure 3: Speckle flow index map (SFI) 15

Figure 4: Representative SFI maps 16

Figure 5: Molar extinction coefficients of oxygenated and deoxygenated hemoglobin 18

Figure 6: Example of hemoglobin saturation map of vessels within a dorsal window chamber 20

Figure 7: Mouse model exposed to an exterior light source during fluorescence imaging 22

Figure 8: Schematic drawing of our imaging system 25

Figure 9: Illumination sources used during imaging 26

Figure 10: Side view of the motorized filter wheel 27

Figure 11: Imaging mount used to fix the window chamber onto a microscope stage 28

Figure 12: Anesthesia nose cone mounted on a microscope stage 29

Figure 13: An air stream incubator 30

Figure 14: A light-tight enclosure system 31

Figure 15: A Bright field image taken prior to laser treatment 33

Figure 16: Representative SFI maps obtained from a mouse dorsal window chamber 34

Figure 17: A syringe-based infusion pump (left) and
PDMS made flow phantom (Right) 36
Figure 18: Schematic representation of our flow phantom experiment 37
Figure 19: Raw speckle contrast map acquired from our flow phantom 38
Figure 20: Measured speckle contrast as a function of actual flow spee 39
Figure 21: Relationship between the computed mean
SFI values and the varying flow speeds 40

ACKNOWLEDGEMENTS

First and foremost, I would like to express my deepest gratitude to my advisor, Professor Bernard Choi who jumpstarted my passion for research by allowing me to be a part of his amazing research group. His tireless mentorship, guidance and support helped me enormously throughout this journey.

My appreciation also extends to my committee members, Professor Elliot Botvinick and Dr. Kristen Kelly for their precious time and commitment.

I would also like to thank Dr. Wangcun Jia who has helped educate and train me in various aspects of my dissertation research. Lastly, I would like to thank the Microvascular Therapeutics & Imaging (MTI) Laboratory for their support and contribution throughout the course of this work.

ABSTRACT

By
Bita Kianian

Master of Science in Biomedical Engineering

University of California, Irvine, 2017

Professor Bernard H. Choi, Chair

Port wine stains (PWS) are congenital vascular malformation of the skin that occur in 3-4 infants per 1000 live births. A major factor that contributes to treatment failures of Port wine stain (PWS) birthmarks is reperfusion of photocoagulated blood vessels due to wound healing response. The study of physiological processes that govern the microvasculature plays a major role in our ability to discover solutions toward enhancement of the current treatments to port wine stain and many other diseases. The functionality of microvasculature and their response to external influences is difficult to assess with the traditional analysis techniques such as histology. The work described in this thesis aims to provide a microvascular optical functional imaging solution specifically designed for use with the rodent dorsal window chamber models.

Our microvascular imaging system was designed to obtain images with three different imaging modes: Laser speckle imaging (LSI), Multispectral Imaging/Oxygenation imaging (MSI/O2I) and Fluorescence imaging (FI). Each of these imaging techniques provides information about the different aspects of microvessels. LSI is utilized to measure the relative changes in blood flow, MSI enables computation of hemoglobin saturation maps, and FI highlights biochemical processes active in a subject. Our analysis showed that the developed imaging system that combines different imaging techniques could be used as a valuable tool to assess the behavior of microvessels over time in response to external factors.

CHAPTER 1 –Background and Significance

1.1- What is a port wine stain?

Port wine stains (PWS) are a congenital vascular malformation of the skin that occur in 3-4 infants per 1000 live births.[1] They are characterized as pink-red to purple demarcated patches on the skin that are caused by an abnormality of capillary vessels.[1] Although the origin and pathogenesis of PWS is not fully understood, the GNAQ mutation is now thought to be central to development.[2]

There are two subtypes of microvascular abnormalities. Type I consists of superficial, tortuous, dilated end-capillary loops in the superficial papillary dermis that appear to be more responsive to laser therapy than type II lesions. Type II lesions have dilated vessels in the superficial horizontal vascular plexus that are deeply located and they appear to be more resistant to PDL treatment.[1]

In general, PWS is a clinically progressive disease with potentially destructing psychological and physiological complications. PWS may also be indicative of a larger disorder or syndrome such as Sturge-Weber syndrome (SWS), Klippel-Trenaunay(KTS) and Cobb syndrome. Each year, about twenty million individuals worldwide and 900,000 people in the United States have PWS birthmarks.[2] While these lesions can occur in any cutaneous site, approximately 90% of all port wine stains occur in the head and neck regions that make up less than 14% of the total body surface.[3] Although they can seem harmless, PWS can enlarge and gradually become darker in color over time. If left untreated, these birthmarks can lead to other deformities and health complications including nodularity, dental abnormalities, soft tissue hypertrophy, and vessel

malformations in other organs of the body such as brain and eyes.[3] [4]About ⅔ of patients with PWS are expected to develop complications such as soft tissue hypertrophy and cutaneous nodules that may bleed and lead to cosmetic disfigurements, prompting many patients to seek treatment.

1.1.2 -Current Therapies in The Treatment of Port Wine Stain

In the past, treatments such as excision with skin grafting, ionizing radiation, electrotherapy, dermabrasion, and cryosurgery were used to treat PWS lesions. [5]However, these treatments often do not result in complete removal and are associated with significant discomfort.[4] Currently, vascular-specific laser irradiation, most prominently pulsed dye laser (PDL) comprises the clinical gold standard treatment of PWS birthmarks in the US. [6]

PDL is a vascular-specific laser system that conforms to the principle of selective photothermolysis of Anderson and Parrish.[7] The theory describes a method that selectively destroys subsurface targets without causing any unwanted thermal damage to the surrounding normal tissues.

There are four ways that light can interact with the target tissue: reflection, absorption, scattering, and transmission. The target tissue remains unaffected when the light is reflected, transmitted or scattered. [7] However, absorption of the light generates heat that can be confined. The heat confinement causes irreversible damage to the target tissue region.

Once the laser energy is absorbed by tissue substance, three important biological responses can occur: photomechanical, photochemical and photothermal. Photomechanical effects occur when very high energies are absorbed in a very short pulse duration, leading to rapid thermal expansion and subsequent photomechanical destruction of the tissues.[11] [8] Photochemical

reactions occur when light is absorbed by a chemical substance. An example of photochemical reaction can be seen in photodynamic therapy (also known as PDT) in which endogenous and exogenous photosensitizers that serve as chromophores become activated by absorbed light for a specific length of time. The activated photosensitizers convert the light into a photochemical reaction. In the presence of oxygen, the photochemical reactions generate cytotoxic reactive oxygen species. If the photosensitizers are intravascular, these species can cause thrombosis and vessel occlusion. [8 11]

Lastly, photothermal reactions occur when the absorbed light by the target chromophore is transformed into heat, leading to irreversible thermal damage and thrombosis to the target structure and ideally minimal effect on the neighboring structures. [9] An example of photothermal reactions can be seen with vascular PDL therapy, which aims to achieve complete photocoagulation of the target vessels leading to an optimal elimination of vascular lesions, while minimizing collateral damage to the neighboring dermal and epidermal structures. [10] The main principle that allows the PDL to selectively destroy PWS ectatic capillaries is known as selective photo-thermolysis.[11] Photo-thermolysis is a unique technique which relies on the selective absorption of brief laser pulses that selectively destroy target structures at the cellular, ultrastructural or tissue structural level.[12]

1.2 - Selective photo-thermolysis

Through selective photo-thermolysis, the monochromatic yellow light transmitted by the PDL is absorbed to a high degree by the target structure or chromophore.[9] Chromophores are defined as covalently bonded molecules that are present in the tissues and are responsible for their color.

These molecules are able to absorb a certain wavelength of visible light based on their absorption coefficient and reflect the other wavelengths, thus producing a color. The most common chromophores in the skin are oxyhemoglobin, deoxyhemoglobin and melanin.[13]

The main goal of photo-thermolysis is to deliver specific wavelengths that match with the last peak in the absorption spectrum of the target chromophore (oxy-hemoglobin in the case of vascular lesion treatment). Moreover, the selected wavelength should be far from the absorption spectrum of competing chromophores (melanin in the case of vascular lesions treatment). Studies have shown that with PDL treatment, the vast majority of patients have had significant improvement of the PWS, meaning lightening of at least 25 to 75 percent. [14]

Each patient has unique skin color and each birthmark has a slightly different vessel pattern. Therefore, in order to achieve optimal clearance of the birthmark. laser parameters should be selected on an individual basis. Parameters that can be adjusted include wavelength, pulse duration, and the amount of the delivered energy (fluence).

Fundamentally, the selection of laser light wavelength corresponds to the absorptive characteristics of the chromophore of the target structure. The three absorption peaks corresponding to the primary chromophore of the skin (again oxyhemoglobin in the case of vascular lesions treatment) are in the visible range of electromagnetic spectrum at 418, 542, and 577 nm.[15]

In addition to wavelength, the exposure time or pulse duration is another important factor. Pulse duration is mainly guided by the target vessel's thermal relaxation time. Thermal relaxation time (TRT) is defined as the time required for the target structure to dissipate 63% of its temperature.[11] Thermal relaxation time is proportional to the square size of the target chromophore. In order to limit the amount of heat diffusing into the neighboring tissues, the

pulse duration has to be matched with the diameter of the target vessels that is being treated. Early pulsed dye lasers used a laser wavelength at 577 nm and a pulse duration of 300 μs for treatment of the PWS, which effectively damaged vessels without evidence of unwanted thermal damage to the surrounding tissues.[16] However, modifications in the form of a longer wavelength (585 - 595 nm) and a longer pulse width (450 μs to 40 ms) have been introduced to enhance lesion clearance. [12]Additionally, a sufficient fluence or energy density (7 to 15 J/cm^2) is needed achieve adequate photocoagulation. Current PDL systems with longer wavelengths are able to achieve deeper dermal penetration, while maintaining vascular specificity. Moreover, the use of longer wavelengths provides decreased epidermal melanin absorption of light. Melanin, which is mostly present in the epidermis is identified as a competing absorber of light during the laser treatment of PWS. The absorption of light by melanin reduces the amount of radiant exposure that can be delivered to the PWS blood vessels. Moreover, it causes thermal injury to the epidermis and can result in complications such as scarring, dyspigmentation or blistering.[17]
While PDL is an effective treatment for PWS, there are potential limitation in terms of treatment efficacy that prevents the complete clearance of lesions. The effectiveness of selective photo-thermolysis depends on the PWS vessel geometry and anatomy, epidermal pigmentation[18], dermal scattering, blood concentration, and the blood vessel configurations. [6]
Some of the factors that contribute to treatment failures of PWS include high melanin concentration, which reduces the light penetration to the targeted vessels, presence of small diameter PWS vessels(<20μm) that leads to a partial photocoagulation of target vessels due to poor thermal confinement, and reperfusion of photocoagulated blood vessels as a result of the wound healing response .[19 20 21]

1.3- Angiogenesis and Vasculogenesis After PDL-Treatment

PDL irradiation of PWS skin induces an acute damage to blood vessels and results in a severely hypoxic microenvironment (having low oxygen levels). However, the wound repair response of human skin triggers a defense mechanism in response to local hypoxia. This often leads to reformation and reperfusion of the PWS blood vessels within a month of the laser therapy.[22] Wound healing is a complex process in which our body attempts to restore normal structure and function in response to an injury.[23] In order for our body to restore its normal structure, it requires new blood vessels that can carry variety of mediators, nutrients and signals.[24] Blood vessels can be formed via two distinct mechanisms: vasculogenesis and angiogenesis. Vasculogenesis refers to development of new blood vessels by aggregation and vascular morphogenesis of endothelial cells. During vasculogenesis, endothelial progenitor cells differentiate into angioblasts, which then aggregate into solid vascular cords, resulting in formation of the vascular plexus. [25]

Angiogenesis, on the other hand, denotes the outgrowth of capillary buds and sprouting of new blood vessels, which happens from pre-existing blood vessels, in response to an injury. [26]

Change in oxygen level result in upregulation of hypoxia inducible factor -1alpha (HIF-1α). HIF-1α is an oxygen-sensitive subunit of HIF-1, which plays a crucial role in the body's response to an oxygen deprived environment. One important function of HIF-1α is to control the expression of genes that are involved in the angiogenesis process. In hypoxia, HIF-1α binds to the regulatory region of pro-angiogenic factors such as vascular endothelial growth factor (VEGF), Fibroblast growth factor 2 (FGF2) and platelet-derived growth factor beta polypeptide (PDGFB).These angiogenic growth factors are controlled by HIF-1α at the transcriptional stage and mTOR/S6 kinase signalling at the translational stage.[46] These growth factors are released

into the extracellular environment between cells, where they can bind and activate their receptors including Fibroblast growth factor receptor 2 (FGFR2), Vascular endothelial growth factor receptor 2 (VEGFR2), FMS-like tyrosine kinase 1 (FLT1), and PDGF receptor, alpha polypeptide (PDGFRA), on adjacent cells.[27] Following receptor activation, several angiogenic signaling pathways get activated. These signaling pathways include protein kinase C (PKC), phosphatidylinositol-3-kinase (PI3K)/AKT, protein tyrosine kinase 2 (PTK2), SHC trans-forming protein 1 (SHC1)/mitogen-activated protein kinase (MAPK), and endothelial nitric oxide synthase 3 (NOS3). Activation of these signaling pathways play integral roles in cellular processes of proliferation, migration, survival as well as blood vessel stabilization that contributes to angiogenesis.[26]

Vasculogenesis is another important mechanism that may be involved in reformation and reperfusion of photocoagulated blood vessels. Scientific evidence has demonstrated that circulating endothelial stem cells (characterized by surface expression of CD133) and mesenchymal stem cells (characterized by expression of CD166) can be recruited into skin sites where blood vessels are photocoagulated. These studies suggest that vasculogenesis also plays an important role in regrowth and reperfusion of destroyed vessels after PDL therapy. [22]

CHAPTER 2: Optical Imaging

The study of physiological processes that govern the microvasculature enables discovery of solutions toward development of new therapeutic strategies to many diseases. However, the functionality of microvasculature and knowledge of its response to external factors is difficult to assess with traditional analysis techniques such as histology. Microvascular optical imaging has proven to be a valuable tool for assessing the microvascular response over time to external factors.[27]

The work described in this thesis aims to provide a microvascular optical functional imaging solution specifically designed for use with the rodent dorsal window chamber model. Dorsal window chamber models have been used during the last two decades to study microvasculature *in vivo.* The window chamber model provides useful information related to the development of hypoxia, angiogenesis, vascular function, tumor microenvironment and treatment responses. [28]

2.1- Rodent dorsal window chamber model

Dorsal window chamber model is well suited for applications that necessitate use of high-resolution imaging of dynamic processes. [28] With this technique, we previously gathered insights into the mechanisms associated with angiogenic and inflammatory response to laser irradiation, as well as changes that occur in blood oxygenation level after laser irradiation. Moreover, in vivo imaging of window chamber models has provided us with insight into the dynamic processes that

modulate the structure and function of the microvasculature. Figure 1 depicts a rodent dorsal skinfold window chamber model that was used in this thesis research.

.

Figure 1 : Rodent dorsal skinfold window chamber model

The installation of titanium dorsal window chambers on C3H mice was carried out under a protocol approved by the Institutional Animal Care and Use Committee at the University of California, Irvine. All equipment was prepared and sterilized before anesthetizing the mice. Mice were initially anesthetized with isoflurane gas and anesthesia was maintained with 80-100 mg/kg Ketamine, 10-12.5 mg/kg Xylazine, and saline solution through an i.p. injection; additional anesthesia was injected as needed during the surgery. The surgeries were performed on heating pads, and the temperature and breathing rate of the animal were monitored every 15 minutes. The following describes the surgical procedure on a typical animal. Sterile ophthalmic ointment was applied to both eyes to keep the cornea lubricated. Electronic clippers were used to remove the majority of dorsal hair; commercial depilatory cream was then spread over the skin to

remove any remaining hair. The cream and any residual hair were washed off with wet paper towels and alcohol pads. The dorsal skin was then gently stretched and trans-illuminated with either a white or green light source to facilitate selection of vasculature to be included in the window chamber. The chamber frames were centered on the desired vasculature—one frame on each side of the skin—and sterile 16-gauge needles were inserted through the three screw holes in the chamber frames to create spaces in the skin for the screws. A small pair of hemostats was used to stretch each channel by placing the hemostats through the channel and gently opening the hemostats.

The front window chamber was prepared by inserting the screws into the three screw holes, and then the plastic spacers (about 4 mm in length) were fit onto each of the three screws. The front chamber frame was placed onto the dorsal skin so that the three screws were inserted into each of the three holes, ensuring that the skin did not extend past the spacers (i.e. the skin is not in contact with the screws). The back-chamber frame was secured on the other side of the dorsal skin with washers; note that the back half of the window chamber should contain the skin with the vasculature to be examined. The washers were tightened enough—compressing the spacers—for the frames to immobilize the dorsal skin without pinching it. In the corresponding suture holes, the frame was sutured to the dorsal skin at all four corners.

With forceps and micro-scissors, the upper layer of skin and all subcutaneous fascia was removed from the front window chamber, leaving only the layer skin with the desired vasculature. About 1 to 1.5 mm of skin was left along the edges of the window frame to prevent future leakage of saline. The window chamber was filled to volume with sterile saline to avoid

air bubbles; a glass coverslip was carefully wiped with alcohol pads to remove any particles and was set on top of the window chamber, which was then secured with a plastic C-holder. Analgesics (0.05-0.10 mg/kg Buprenorphine) were promptly administered through an i.p. injection. The mouse was immediately irradiated to the targeted vessels, and then imaged on days 0 (day of irradiation), 1, 3, 5, 7. After imaging day 7, the mouse was euthanized through a Euthasol i.p. injection primary and a spinal dislocation secondary. Window chamber frames, screws, and washers were all cleaned and sterilized for future use.

2.2 - Imaging Modalities

With respect to imaging, there are various imaging techniques that can be used to monitor the microvasculature within the dorsal window chamber. We integrated three different imaging modalities into a system that could be used as a tool to monitor and assess microvascular architecture, blood flow dynamics, and blood oxygenation levels. Our microvascular imaging system was designed to obtain images with three different imaging modalities: Laser speckle imaging (LSI), Multispectral Imaging/Oxygenation imaging (MSI/O2I) and Fluorescence imaging (FI). Each of these imaging techniques can give us insights related to different aspects of the microvasculature. LSI is a technique that can be used to monitor the changes of blood flow and enable generation of *in vivo* maps of relative blood flow or what we call speckle flow index (SFI) maps.[25] MSI/O2I is another imaging technique that can be used to create oxygenation maps of vasculature to assess the changes of oxygen saturation within the blood vessels in response to external factors such as selective laser injury. FI was integrated into our system to enable imaging of fluorescent molecules such as indocyanine green and fluorescein derivatives in current and future work.

2.2.1 Laser Speckle Imaging (LSI)

Laser Speckle Imaging (LSI), also known as laser speckle contrast imaging, is a technique that involves analysis of the speckle pattern that results from laser light illumination of a sample. The laser light remitted from the sample creates a random granular effect known as a speckle pattern. The speckle pattern is a randomly varying intensity pattern that is formed due to constructive and destructive interference of coherent laser light that is scattered by an inhomogeneous sample. The resulting interference pattern can be used to study the movement of scattering particles within the illuminated tissue. The movements of scattering particles can be quantified by evaluating either temporal or spatial variations. If the sample is static, the speckle pattern remains unaltered over time. However, if the sample contains moving optical scatterers such as particles in a fluid, the speckle pattern becomes time-varying.[30] By capturing reflectance images of speckle patterns at a predetermined integration time (exposure time), we can identify regions of dynamic activity in a sample. It is the premise of LSI to assess the degree of blurring or resulting loss of contrast and correlate it to dynamic activities such as blood flow, in the case of microvasculature.

Moving scatterers such as red blood cells blur local regions of the speckle pattern captured with a CCD or CMOS camera, as opposed to the relatively high contrast speckle pattern associated with static regions. An example of a bright-field image (Figure 2-left) as well as a raw speckle image (Figure 2-right) obtained from a rodent dorsal window chamber is shown below. Note that the blurred regions within the raw speckle image represents the presence of blood flow within

vessels and the regions in which the speckle pattern does not appear blurry correspond to an absence of blood flow. We note that the speckle pattern created by the laser is not perfectly static and it gradually fluctuates in time at a rate proportional to the speed of moving particles. Therefore, if these fluctuations occur during the exposure time of the camera, the associated regions in the image appear blurry.

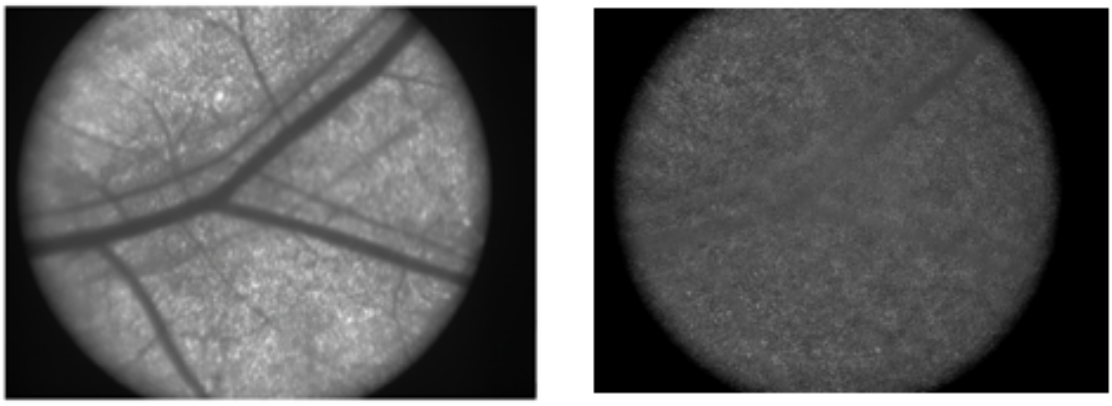

Figure 2: Bright-field reflectance image (Left) and raw speckle image (right) of microvasculature within a dorsal window chamber. Note the blurred regions in the raw speckle image correspond to vessels with blood flow in the reflectance

The degree of spatial variance or blurring of the speckle pattern can be quantified at each pixel as a speckle contrast value, denoted as K.

K is defined as the ratio of the standard deviation(σ) and the mean intensity (<I>) of the pixels within a local region. It is computed by the following equation:

$$K = \frac{\sigma}{<I>} = \frac{\sqrt{[1/(N-1)]\sum_{i=1}^{n}(I_i - <I>)^2}}{<I>} = \frac{\sqrt{[1/(N-1)]\,(\sum_{i=1}^{N}((I_i)^2 - N<I>^2)}}{<I>}$$

Equation 1

where σ is the standard deviation of the speckle intensity, <I> is the average intensity of pixels, N is $(\omega + 1 + \omega)^2$ where ω is radius size of the window, and I_i is the intensity of pixel i within the sliding window.

This equation is calculated over a sliding window of 5x5 or 7x7 pixels surrounding each pixel of the raw speckle images, resulting in full field speckle contrast maps. According to Le at al., the size of the sliding-window is an important parameter to consider when calculating speckle contrast value as selecting a window that is too small in size reduces the sensitivity to vascular variations, and a too large window can result in the loss of effective resolution. [31]

Speckle contrast value K is also inversely proportional to flow speed and ranges on a scale from 0 to 1, where 0 corresponds to larger motion of optical scattering particles and high blurring of speckle pattern, and 1 corresponds to regions with no movement of scattering particles and speckle pattern is completely developed.[32]

After computing the speckle contrast images, we create speckle flow index (SFI) maps to visualize blood flow dynamics. To quantify SFI, the speckle correlation time (τ) is computed using the following equation (Eq. 2) derived by Ramirez-San Juan et al and Cheng and Duong. This equation is a simplification based on the assumption of a Lorentzian velocity distribution. [33] [34]

$$\tau = 2TK^2$$

Equation 2

where T is the exposure time in s. Assuming SFI to be directly proportional to the speed of blood flow and inversely proportional to τ at each pixel, we use the following equation to calculate SFI:

$$SFI = \frac{1}{2TK^2}$$

Equation 3

Figure 3 represents an example of a SFI map corresponding to the raw speckle image in Figure 2, calculated using (Eq. 3).

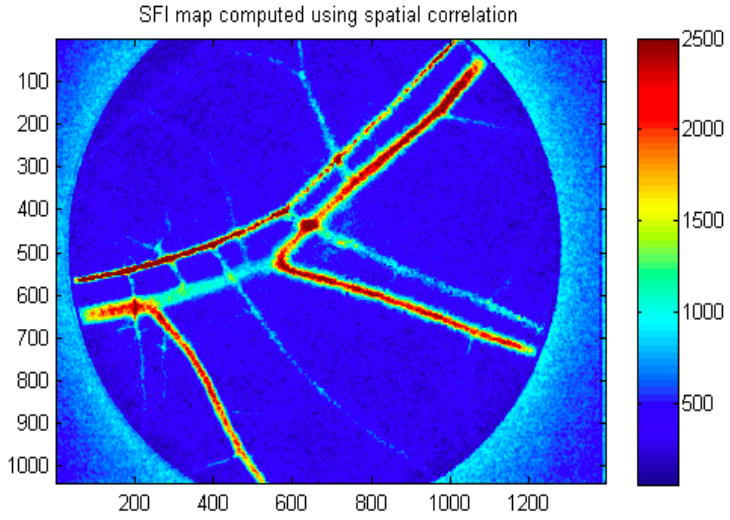

Figure 3: Speckle flow index map (SFI) computed from the speckle contrast map (Fig 2, right) using spatial correlation. [units: s^{-1}]

Exposure time associated with the raw speckle images is another important parameter that can alter the sensitivity of LSI to different perfusion velocities. In order to sense the slower blood flow in smaller caliber vessels such as venules and capillaries, longer exposure time is required. The use of long exposure time during LSI imaging increases the sensitivity of K to relatively smaller blood flows in the region of interest.[35] However, use of longer exposure times increases the speckle contrast noise and decreases the imaging contrast K for higher flows. Therefore, long exposure times are only appropriate for visualizing the structure of the vessels rather than quantifying the blood flow within the vessels.

For this experiment, we selected exposure times of 10 and 1000 ms, which allowed us to identify vessels with different ranges of flow speed in both larger and smaller vessels within the rodent dorsal window chamber.[35] Figure 4 compares the SFI maps taken at two different exposure times of 10 (Left) and 1000 ms (Right) that are computed from the corresponding speckle contrast maps (Fig 2b).

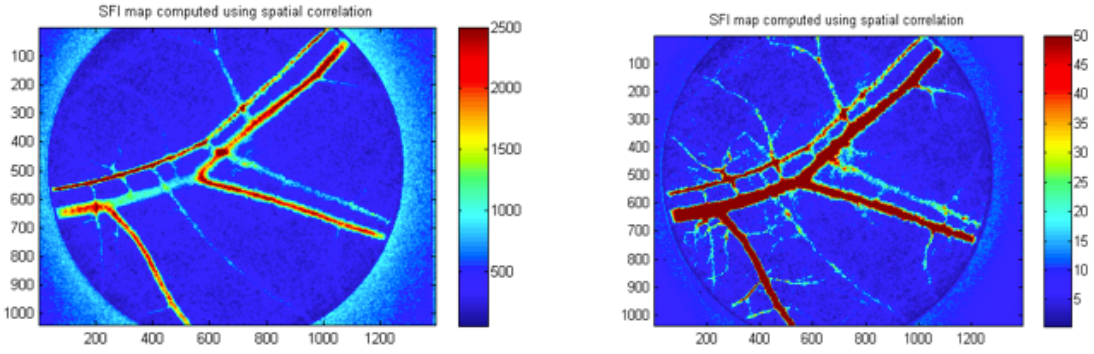

Figure 4: Representative SFI maps determined from speckle images collected with exposure times of 10 (left) and 1000 ms (right). Note the increase in discernible vasculature in blood flow maps taken with a longer exposure time (ie. 1000 ms)

The LSI instrument is comprised of a few basic components. A laser diode with a center wavelength of 785 nm (Ondax SureLock 785 nm wavelength stabilized laser, Monrovia, California) for illuminating the sample, a high performance Retiga 2000R (QImaging, Burnaby, BC, Canada) 12-bit color-cooled camera with a resolution of 1600 (W)×1200 (H) pixels and a zoom lens for detection of reemitted light and imaging optics to focus the laser light that has been directed onto a region of interest on the camera sensor. [36 37]

During LSI, the dorsal window chamber of an anesthetized mice was trans-illuminated by the laser diode (Ondax, Monrovia, California) which serves as a coherent source for our LSI

experiment. Trans-illumination configuration was chosen over epi-illumination because it provides a higher spatial resolution in the dorsal window chamber due to the forward-scattering nature of the red blood cells in the directly imaged microvasculature. To generate speckle contrast maps, we use spatial correlation analysis, which necessitates the acquisition of a series of raw speckle images from the region of interest. To generate speckle contrast maps, we use spatial correlation analysis. Typically, 10 raw speckle images were acquired at exposure times of 10ms and 1000ms. By averaging the computed contrast images at each exposure time, we decrease the speckle noise. The resultant image is then used to generate SFI maps using equation 3. All image processing was performed using custom-written MATLAB software

2.2.2 Multispectral Imaging /Oxygenation Imaging

Multispectral Imaging (MSI) is an imaging technique, which is capable of classifying similar materials both spatially and spectrally, based on their distinct features. One major application of MSI is oxygenation imaging or acquisition of hemoglobin saturation maps. Oxygen in the bloodstream is transported via hemoglobin molecules that consist of four subunits. Each subunit has a co-factor called heme that can bind to an oxygen molecule. [38] To the naked eye, oxygen-poor, venous blood appears darker than oxygen-rich, arterial blood due to the difference in color between oxyhemoglobin and deoxyhemoglobin. MSI enables us to measure this discrepancy based on the light absorption spectra differences between oxygenated and deoxygenated blood. Figure 5 depicts the oxyhemoglobin and deoxy-hemoglobin spectra in terms of molar extinction coefficient.[39]

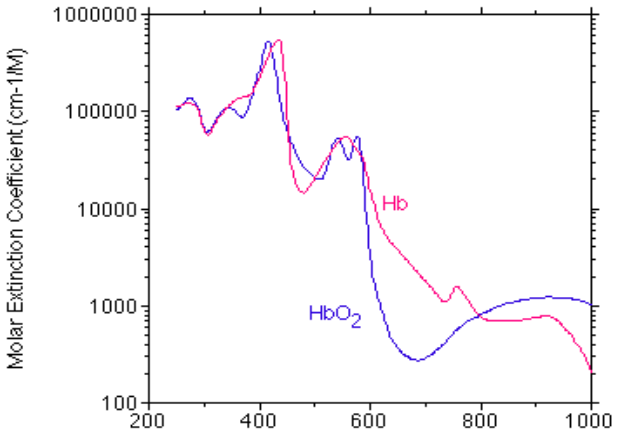

Figure 5 :Molar extinction coefficients of oxygenated (HbO_2) and deoxygenated (Hb) hemoglobin as a function of wavelength.

Oxygen saturation levels define the degree to which hemoglobin molecules in the bloodstream carry oxygen as a percentage of the maximum it could carry (i.e. 100% oxygen saturation indicates that maximum oxygen is carried by the hemoglobin molecules).[40] The amount of light absorption by blood can be used to calculate the oxygen saturation levels in the blood stream.[41] In order to quantify vascular oxygenation, a multispectral imaging system was integrated into our imaging system. The schematic representation of the MSI imaging setup is depicted in Fig 8. MSI imaging is accomplished by using a few key components which include, a high-performance CCD camera (Retiga 2000R, QImaging, Burnaby, BC, Canada), a 0.7x high resolution microscope adapter (HR 0.70-CMT, Spot Imaging / Diagnostic Instruments, Inc.) coupled with a bottom clamp to mount the camera to the microscope. A FW102C automated filter wheel that accommodates six ø1″ circular filters (510 nm, 540 nm, 600 nm, and 632 nm)

was located in front of the camera. If required, the whole wheel can be quickly detached and replaced allowing for fast swapping of entire filter-sets. [42]

During MSI, the rodent dorsal window chamber was trans-illuminated via a LED source (ANSI white Luxeon Rebel ES LED) that was driven at 700mA. Detection was made using a CCD camera with a six-position filter wheel in the path.

In this experiment, oxyhemoglobin and deoxyhemoglobin were assumed to be the dominant absorbers in blood. Five different band pass color filters centered at wavelengths (nm) of 510, 540, 600,632 nm was selected. These wavelengths were selected based on the wavelength-dependent absorbance of hemoglobin.[44] Selection of multiple wavelengths throughout the visible spectrum allows us to measure the discrepancy in oxyhemoglobin and deoxyhemoglobin. Images were acquired in bright field mode in trans-illumination configuration at wavelength range of 500-630 nm. Depending on the wavelength that was used, the exposure time was adjusted accordingly such that the full dynamic range of the camera was employed.[44] Once the images were collected, we used them to create image cubes (x, y, λ) that could be quantitatively analyzed to compute vascular oxygenation within each vessel in our window chamber model. [28] An example of the hemoglobin saturation map of microvasculature in a window chamber is shown in (Figure 6).

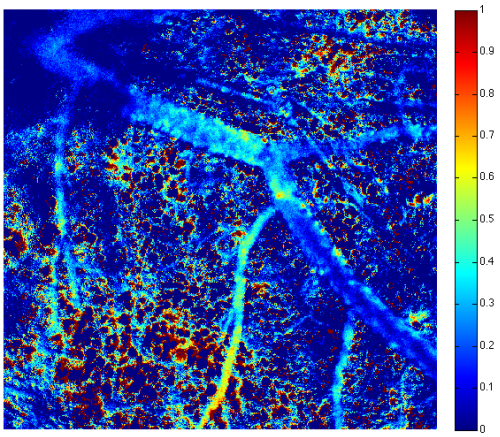

Figure 6:Example of hemoglobin saturation map of vessels within a dorsal window chamber. Note the differing saturation levels (low to high) were color-coded as blue, green, yellow, and red.

2.2.2.1 Generation of hemoglobin oxygen saturation maps

The modified Beer–Lambert law model equation was used to convert the spectral images to images of HbO2 and Hb-R.

$$A_\lambda = log(\frac{I_0}{I}) = \varepsilon_\lambda^{HbO2}\,[HbO2].L + \varepsilon_\lambda^{Hb-R}\,[Hb-R\,].L + S.L$$

Equation 4

which can be re-written as:

$$A_\lambda = [(\varepsilon_\lambda^{HbO2} - \varepsilon_\lambda^{Hb-R}).\,Hb_{sat} + \varepsilon_\lambda^{Hb-R}\,].L.\,Hb_{tot} + S.L$$

Equation 5

Where $Hb_{tot} = [HbO2] + [Hb-R]$ and $Hb_{sat} = Hb_{O2}/Hb_{tot}$

which can then in turn be rewritten as: $A_\lambda = \Delta\varepsilon_\lambda.a + \varepsilon_\lambda^{Hb-R}.b + c$

Equation 6

Where a=Hb_{sat}. L. Hb_{tot}, $b = L\ .Hb_{tot}$ and $c = L.S$

Where A(λ) is the absorbance at wavelength λ, I is the detected light intensity at a given pixel, I_0 is the incoming light intensity selected manually from avascular regions of a tissue, OD is optical density, ε_{HbO2} and $\varepsilon_{Hb\text{-}R}$ are the extinction coefficient of oxyhemoglobin and deoxyhemoglobin respectively. [HbO2] and [Hb-R] are the concentration of oxyhemoglobin and deoxyhemoglobin, respectively, L is the path length traveled by the sampled light, and S is the path length-dependent scattering term.

With this linear mixing model equation, we can calculate the concentration of oxyhemoglobin and deoxyhemoglobin at each pixel using each absorber's extinction coefficients. The extinction coefficients of [HbO_2] and [Hb-R] used in this model equation were taken from Scott Prahl's tabulation of absorption values.[39] Here, we assumed the scattering term (S) to be a constant additive error term over the wavelength range of 500-640 nm.[44] The measured [HbO2] and [Hb] values were then used to compute the oxygen saturation (sO_2) using the following equation:

$$sO_2 = \frac{[HbO2]}{[HbO2]\ + [Hb - R]}$$

Equation 7

A linear least-squares fit was used on equation (7) to compute hemoglobin saturation values. Based on the R^2 value of each pixel (coefficient of determination), the hemoglobin saturation values at each pixel were either accepted or rejected. In our case, pixel fits with an R^2 below threshold of 0.95 were rejected. To avoid any artifacts on the hemoglobin saturation values, it is important to select the same avascular region in each image at each wavelength, and to not

choose any oversaturated pixels. All image processing was performed using custom-written MATLAB software.

2.2.3 Fluorescence Imaging:

Fluorescence imaging (FI) is a powerful technique that uses the phenomenon of fluorescence to identify different features and/or activities such as angiogenic and vessel repair processes, protein localization and signaling pathways, all of which would not be readily observable under normal circumstances. Fluorescence occurs when a sample absorbs light at a certain wavelength and immediately emits that light at a longer wavelength.

Our imaging platform utilizes an inverted fluorescence microscope (Nikon TE800 and Diaphot TMD, Nikon, Melville, NY) that enables imaging of the fluorescent markers. Fundamentally, FI requires a few basic elements, including an excitation light source (mercury or xenon high-pressure bulb, LED or a laser source) in trans or epi-illumination configuration, a CCD sensor for detection of the emitted signal, a specimen with intrinsic or extrinsic fluorophores labels and a filter block to excite the fluorophore(s) of a specimen.

In vivo fluorescence imaging of microvasculature in a rodent dorsal window chamber model is achieved either by using a transgenic animal or with intravascular injection of a dye. For the purpose of our experiments, we used VEGF - green fluorescence protein (VEGF- GFP)

transgenic mice where the animal model emits GFP protein in response to VEGF gene expression. The correlation between VEGF expression and vascular reperfusion and permeability during the healing response after laser injury indicates that VEGF plays a key part in the angiogenesis process. During fluorescence imaging, our animal model is exposed to an exterior excitation light source, represented in green arrows (Figure 7). The excitation bandwidth is passed through a wavelength-specific filter and directed toward the specimen. The excitation light penetrates to the tissue, and excites the source which leads to subsequent emission of photons which scatter throughout the tissue, and generate a surface radiant which is captured by an eyepiece or a detector.

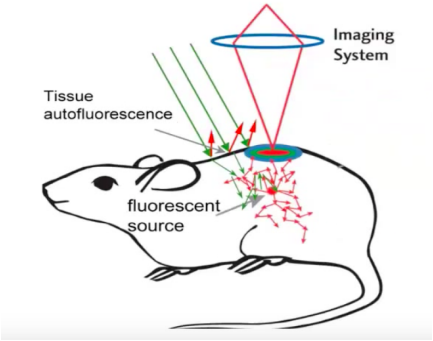

Figure 7: Mouse model exposed to an exterior light source during fluorescence imaging. The light penetrates to the tissue and emits the subsequent photons that scatter throughout the tissue

2.4 – Microvascular Imaging System Walkthrough

Below are tables representing the key components of our multimodal imaging system which includes the optical components, structural components as well as components for animal

support. A schematic representation of the instrument that we designed and built is shown in Figure 8.

Table 1 : List of the key components of our microvascular imaging system that includes optical components, components for specimen support and structural support

Optical components
CCD camera (QImaging, Retiga 2000R)
Intravital fluorescence microscopy (Diaphot TMD, Nikon)
Laser diode (785 nm, Ondax)
Color filters (510 nm,540 nm, 600 nm, 632 nm)
Six-position motorized filter wheel (Thorlabs, Inc.)
Zoom lens
ANSI white LED source (Luxeon star)
2 neutral density filters (OD:4.0 and OD:10.0)

Components for animal support
Isoflurane vaporizer
Anesthesia nose cone
Air stream incubator
Components for structural support
Light-tight enclosure
Window chamber holder
Various optics mounting hardware

.

The imaging system was designed to be a single-platform instrument that would allow for non-invasive, non-contact *in vivo* imaging. It allows for simultaneous measurement of hemodynamic response, molecular fluorescence in tissues, and biochemical composition (i.e. oxyhemoglobin and deoxyhemoglobin).

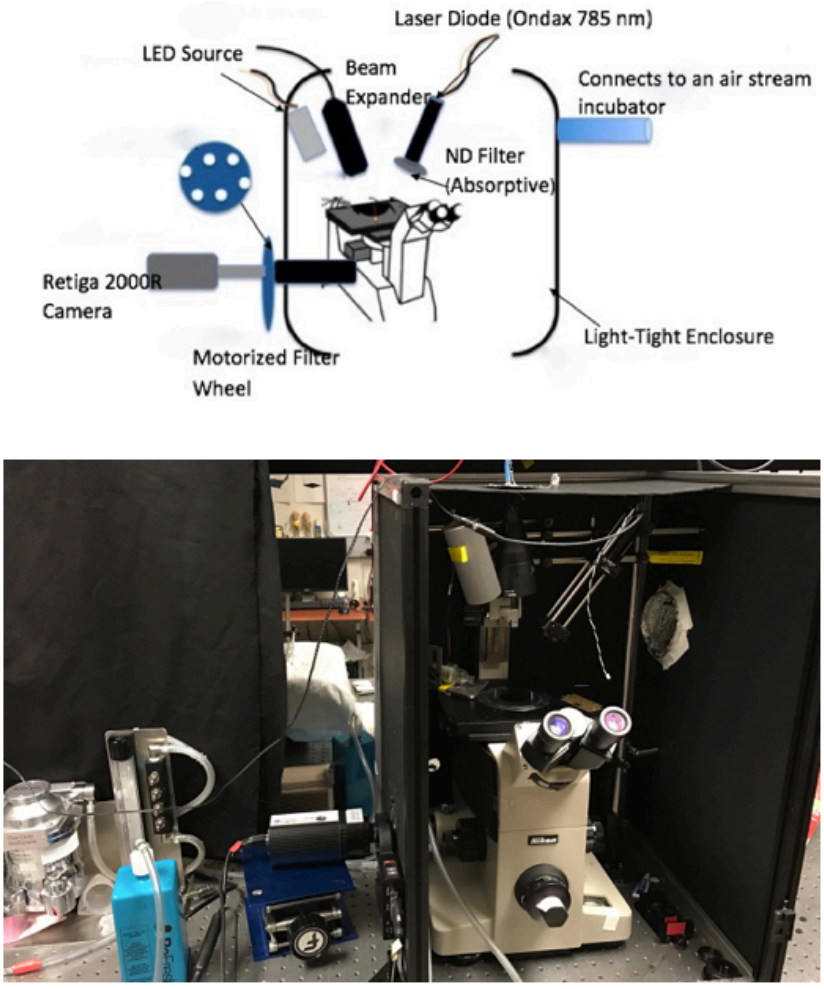

Figure 8: Schematic drawing of our imaging system. Side view of components for LSI, and MSI, and FI imaging (Top figure). An image of the actual imaging system is also shown in bottom figure. A 12 bit monochrome CCD camera (Retiga 2000R) connected to a computer (not shown here) were used for image acquisition.An intravital flurosrence microscope and camera lens was used to assure that beam collimination is achieved. Two illumination sources were brought into use with the imaging system, a 785 nm Ondax benchtop laser for LSI and FI, and a LED source for MSI. A six-position filter wheel loaded with 4 color filters (510nm, 540nm, 600nm, 632 nm) was attached to the camera.

Briefly, the imaging system is comprised of an inverted fluorescence microscope (Nikon TE800 and Diaphot TMD, Nikon, Melville, NY) equipped with a CCD camera (Retiga 2000R, QImaging, Burnaby, Canada) connected to a computer. This camera model was selected for its

low-light sensitivity and compatibility with the MATLAB programming software. Imaging was performed with a Nikon 4x objective (Nikon Plan 4x/0.13 phase microscope objective).

Two illumination sources were brought into use with the imaging system, a 785 nm Ondax benchtop laser (Figure 9) for LSI, and a LED source (ANSI white Luxeon Rebel ES) for MSI and bright-field imaging. Illumination was directed via light guides and optical fibers. A triple output power supply (Hewlett Packard HP 6236B Triple Output Power Supply 0-6V 0-2.5A / 0-20V, 0- 0.5A) was used to power the LED source shown in figure (9). The voltage control knob on the front panel of the power supply enables easy selection of the desired output voltage for the LED source.

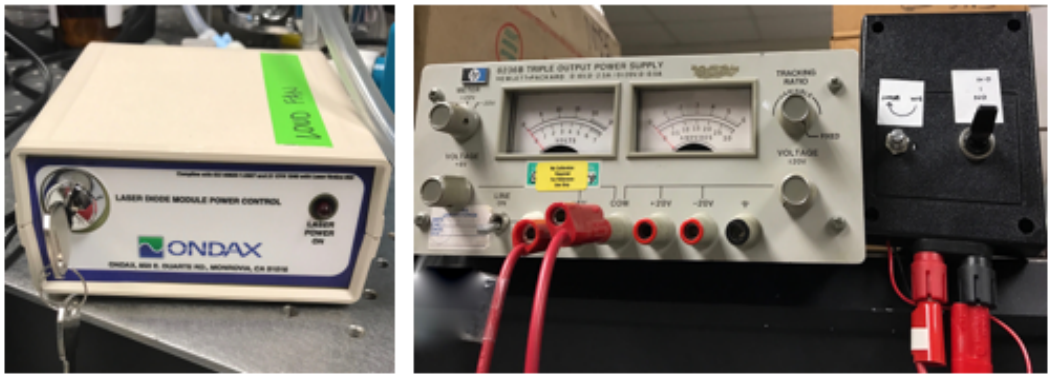

Figure 9: An Ondax benchtop laser feeding the LSI system on the left. A triple output power supply powering up the LED source on the right.

During LSI, laser light was first projected onto a neutral density(ND) filter to attenuate the output light. Depending on the image exposure time, different ND filters with different optical density (NE10A, NE04 A, Thorlabs, Inc.) are placed on the light path of the laser source to achieve the desired light attenuation. The beam was then directed toward the dorsal window

chamber on the microscope stage. Detection was performed using a 12 bit thermoelectrically cooled CCD sensor that was attached to side port of the microscope. The QImaging driver camera was directly controllable with MATLAB's image acquisition toolbox.

During MSI, light from a white LED source was directed towards the dorsal window chamber. A six-position filter wheel loaded with five color bandpass filters was positioned between the camera and the system objective lens via a SM1-CM mount adaptor (Figure 10). The position of the filters was automatically adjusted via computer software (Thorlabs, FW102C).

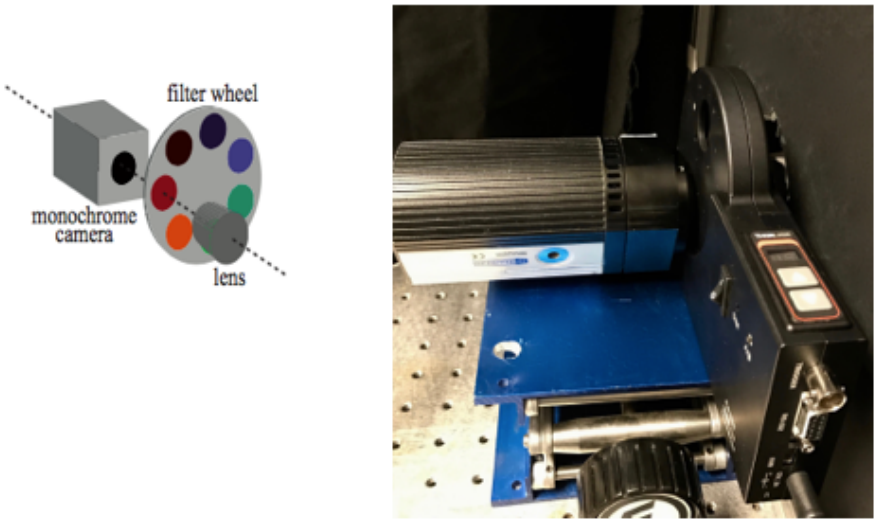

Figure 10: Side view of our motorized filter wheel positioned between the CCD camera and the system objective lens via SMI-CM mount adapter.

The majority of *in-vivo* work in the Microvascular Therapeutics & Imaging Laboratory (MTI Lab) at the Beckman Laser Institute is based on the window chamber model. Therefore, we designed a system that accommodates features that work specifically with window chamber

models. These features include a simple window chamber mounting system, an anesthesia nose cone system, and a heating system.

Window chamber mounting system:

This feature allows for immobilizing the animal subject during imaging sessions (Figure 11). It also leads to a mechanically stable setup that enables consistent imaging on a day-to-day basis. Square imaging brackets were custom tailored to fit within the imaging setup. They consist of a stiff metal with 4 drilled holes. A 12-mm diameter hole was drilled in the center of the bracket, which allowed for direct imaging of the sub-dermal microvasculature of the window chamber. The three surrounding holes (~2 mm diameter) were positioned to allow the window chamber bolts to pass through the bracket.

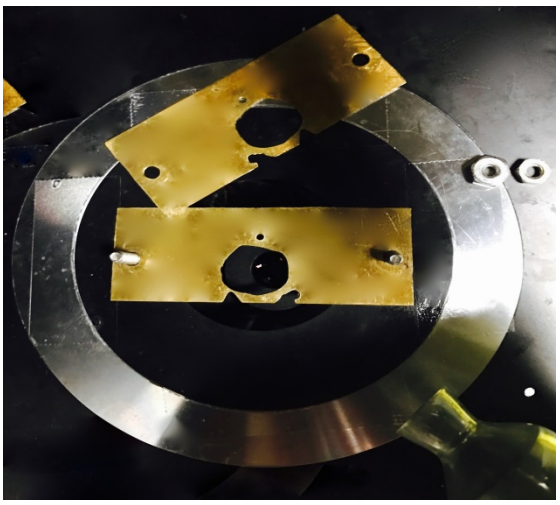

Figure 11: Imaging mount used to fix the window chamber onto a microscope stage. A 12-mm diameter hole was drilled in the center of the bracket to permit imaging, and three surrounding holes (~2 mm diameter) were positioned to allow the window chamber bolts to pass through the bracket.

Two identical square imaging brackets were used. The first bracket was placed on the microscope stage in such a way that the window chamber bolts could pass through. The second bracket was then placed on top to fix the window chamber model. Two external nuts were then

screwed on to the bolts of the window chamber to securely affix the imaging brackets to the microscope stage.

Integrated anesthesia nose cone:

This feature was integrated into our system to keep the animal fully anesthetized for the duration of the imaging session. We used gas anesthesia because it is fast acting and allows for faster recovery. An isoflurane-oxygen mixture was delivered through a nose cone that was mounted on the microscope stage (Figure 12). The nose cone was mounted on a dedicated holder that was easily adjustable. The holder can also accommodate different sized nose cones to fit various rodents such as rats, mice, and hamsters.

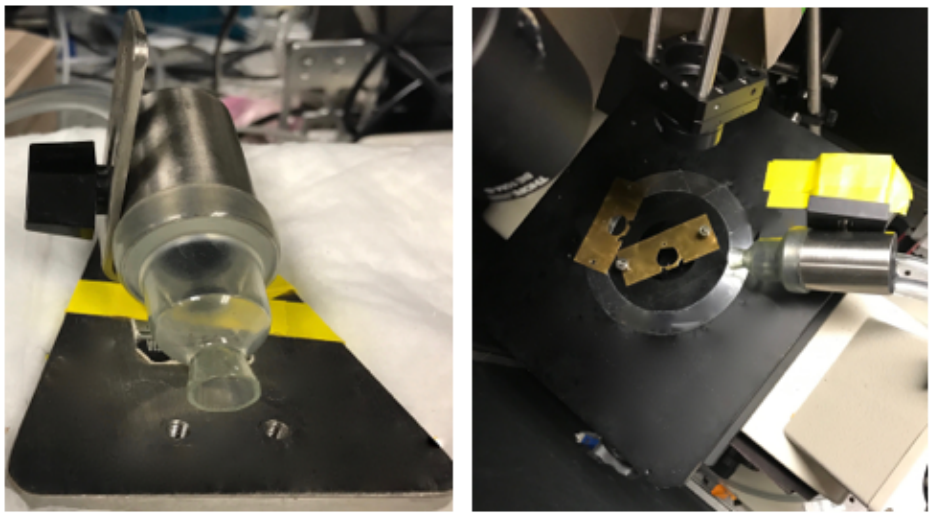

Figure 12: Anesthesia nose cone mounted on a microscope stage via an adjustable holder.

Heating system:

When the animals are kept under anesthesia, their body temperature may decrease and the animal may become hypothermic.[45] Thus, it is crucial to integrate a heating system that would maintain a suitable body temperature during imaging sessions. To prevent a significant decrease of the rodent's body temperature during imaging sessions, we integrated a simple air stream incubator (ASI 400, Nevtek, Williamsville, VA) to our imaging system. (Figure 13) The heat is directed toward the animal subject through a flexible aluminum pipe that is connected to an air stream incubator. (Figure 13) A T-type thermocouple is also mounted onto the aluminum pipe to provide temperature feedback. Since the heater fan generates vibration, it must be kept distant from the microscope.[46]

Figure 13: An air stream incubator (ASI 400m Nevtek, Williamsville, VA) integrated to our imaging setup to maintain a suitable body temperature for the subject under study. The heat was directed toward the subject via a flexible aluminum pipe

Light tight enclosure system:

We integrated a light-tight enclosure system to substantially eliminate ambient light contamination (Figure 14). This feature is specifically beneficial during fluorescence imaging for which low signals can be easily corrupted by ambient light. Essentially, with this feature we optimized the fluorescence detection by eliminating the background ambient light fluorescent signal. This feature also protects the users and other researchers in the lab against the potentially dangerous high-energy laser light that is utilized during imaging sessions. Moreover, incorporating a light tight enclosure to our system allows the laboratory lights to remain on during imaging session that limits the interruption to the work of other researchers in the lab.

Figure 14: A light-tight enclosure system built to eliminate ambient light contamination.

CHAPTER 3: Validation and Applications:

3.1 Long-Term Monitoring of the microvasculature

Long term monitoring of irradiated blood vessels within the window chamber model is crucial for accurate evaluation of the degree of photo injury inflicted on targeted vessels. Typically, short term (<24 hrs.) evaluation of microvascular response to light-based vascular interventions may not persist. Therefore, long term monitoring is crucial for precise assessment of microvascular response to selective injury. Our dorsal window chamber model and optical imaging instrumentation enabled us to perform long term assessment of novel therapeutic strategies designed to alter microcirculation.[47] The surgery was performed on C3H mice, under a protocol approved by the Institutional Animal Care and Use Committee at the University of California, Irvine.

We captured bright-field reflectance images that served as an anatomical reference image (Fig 15) and laser speckle images (Fig 16) that allowed us to monitor the blood flow dynamics of the microvasculature and determine vascular shutdown. A 532nm laser was used to irradiate two arteriole-venule pairs (marked with yellow circles).

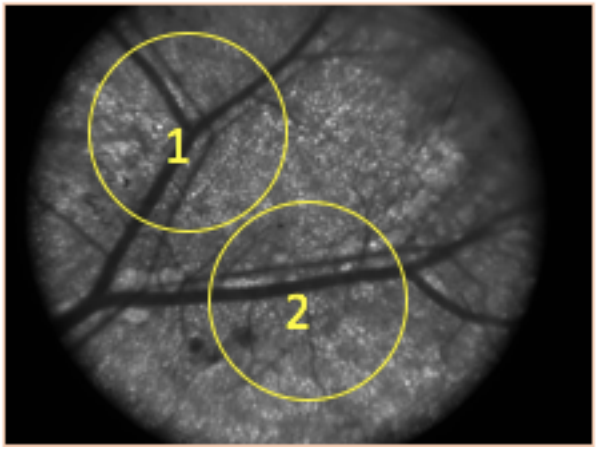

Figure 15: A Bright field image taken prior to laser treatment and served as an anatomical reference image. Vessel segments enclosed in the yellow circle were irradiated with a 532-nm laser.

Laser irradiation parameters used for this experiment was 1 ms pulse duration, 20 Hz repetition rate, and 4.8 J/cm^2 radiant exposure. These parameters were selected based on published results documenting efficacy of these settings for complete photocoagulation of acute vessels.[35] LSI images were acquired from the window chamber model on days 0, 1,2, 3, and 7 (Fig 15).

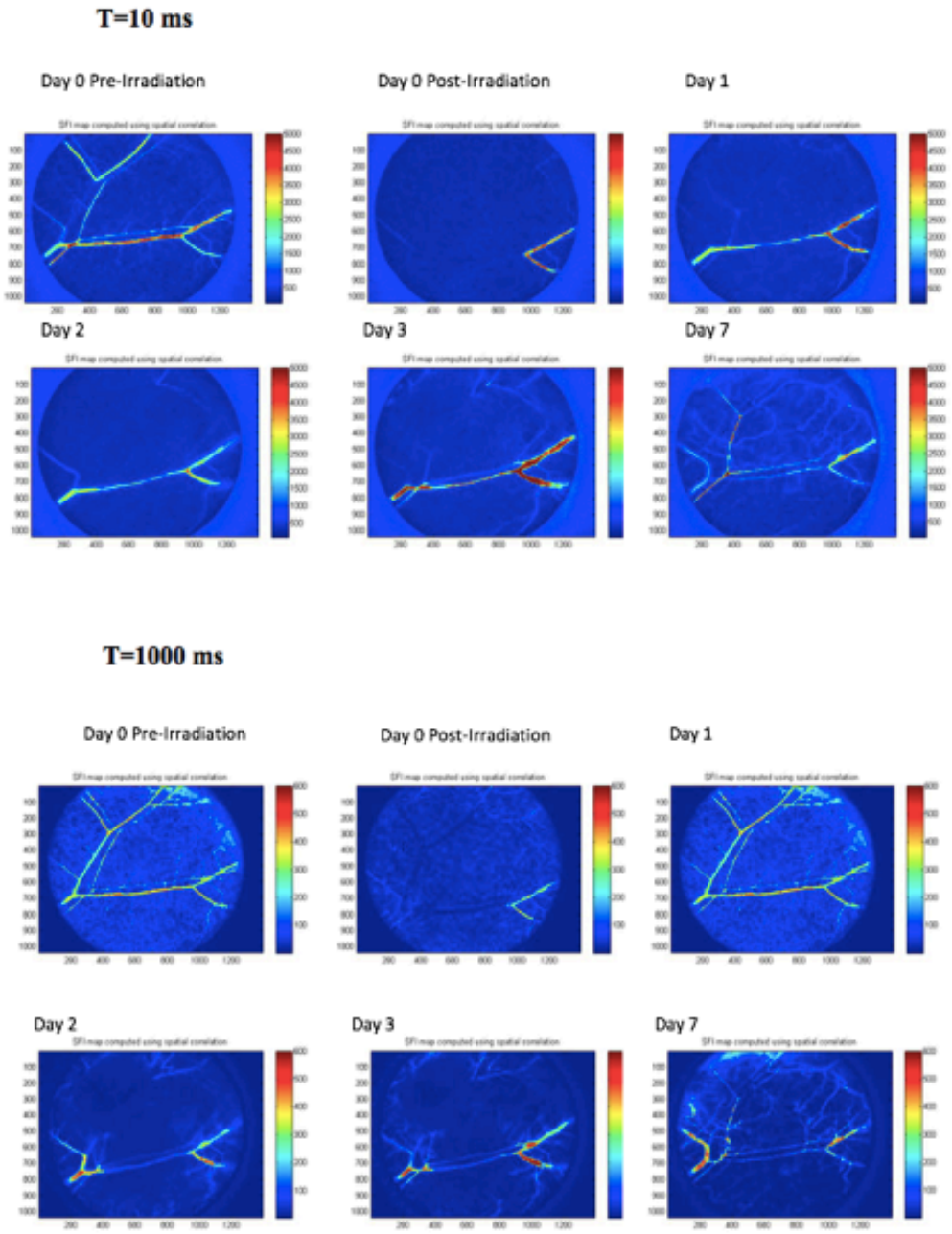

Figure 16: Representative SFI maps obtained from a mouse dorsal window chamber are shown on days 0 (prior and after laser irradiation), 1, 2,3, and 7. LSI was performed using two exposure times of 10 ms (top row) and 1000ms (bottom row) over a period of 7 days after laser irradiation.

The results presented herein (Fig 16) demonstrated vascular reperfusion in the irradiated vessels which was persisted through the end of the monitoring period, indicating that acute vascular destruction may not necessarily result in complete clearance of vascular lesions. Partial to complete restoration of blood flow within the irradiated vessels may be due to incomplete photocoagulation of the target vessels, or an angiogenic/neo-vasculogenic response. In the images obtained one day after intervention we observed a substantial to complete venular flow reduction on one of the irradiated pairs, and a considerable arteriolar flow reduction on the second pair that suggests a complete photocoagulation of selected vessels was achieved after laser injury. However, with subsequent images taken on Days 2, 3 and 7, we saw increased blood flow in the irradiated vessels. Therefore, we hypothesize that posttreatment angiogenesis or neo-vasculogenesis can play a critical role in limiting PWS treatment efficacy by hampering the reduction in dermal blood content.

Furthermore, our LSI system allowed us to visualize the changes that occur to the irradiated and non-irradiated vessels including the vessel repair process, vasoconstriction, vasodilation, and delayed blood flow changes.

3.2 *In vitro* Flow-phantom experiment

To validate the accuracy and stability of our imaging system to collect speckle contrast images, we developed *in vitro* flow phantom experiments. A phantom was used to mimic vascular perfusion and simulate the reduced scattering coefficients as well as absorption coefficient of cutaneous tissue.

The objective of this experiment was to find a relationship between the measured values of the speckle flow index and actual flow rate.[48] As shown in Figure 18, the configuration used for our flow phantom experiments consisted of a few basic elements, including a laser diode that served as a coherent light source (Ondax 785nm), a CCD camera (Retiga) attached to the side port of the inverted microscope (Nikon TE800 and Diaphot TMD, Nikon, Melville, NY), a PDMS flow phantom, a 10 mL BD syringe, a syringe-based infusion pump (Harvard Apparatus, Holliston, Massachusetts), Tygon tubing, and 1% intralipid solution (Baxter Healthcare, Deerfield, IL). Figure 16 was taken from our flow phantom that was constructed out of PDMS with added titanium dioxide nanoparticles (TiO_2) as the scattering agent.[48] The phantom contained a 1.3 mm, inner diameter capillary tube that was embedded at the surface of the PDMS prior to curing, to mimic a blood vessel (Figure 17). The capillary tube was filled with 1% intralipid that was prepared by diluting 0.5 mL of a 20% intralipid solution with 9.5mL of distilled water (1: 19). Intralipid was chosen as a substitute for blood because of its availability and its similar scattering characteristics to blood. With a syringe-based infusion pump, the diluted intralipid solution was pumped through the capillary tube (Figure 17).

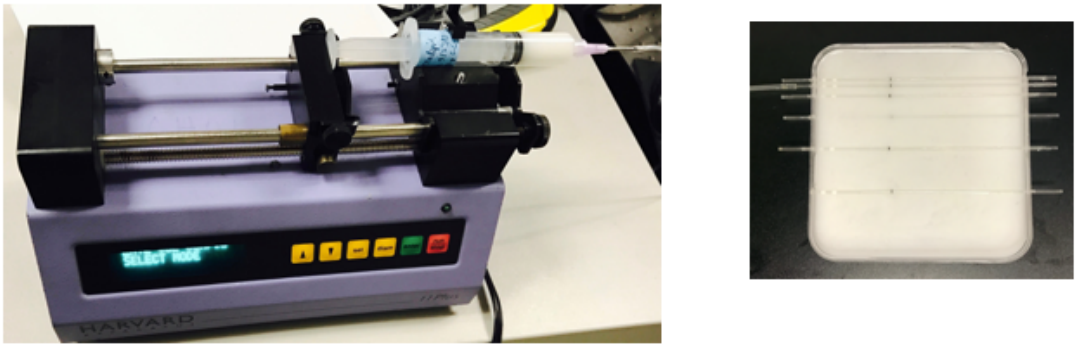

Figure 17: A syringe-based infusion pump loaded with a 10-mL syringe (left figure). The syringe is filled 1% Intralipid solution diluted with distilled water. Image on the right is taken from our PDMS made flow phantom with capillary tubes embedded at the surface of the phantom.

The pump was set to achieve a series of desired flow speeds ranging from 1 to 10 mm/s with 1 mm/s increments, which had to be converted to volumetric flow rates (i.e. ml/min respectively) on the pump. The fluid was directed toward the capillary channels via a Tygon tube that was coupled to the filled syringes to precisely control the flow speed. We also made sure that the pump diameter was set to 14.43 mm, the inner diameter of the syringe that was used to capture solution.

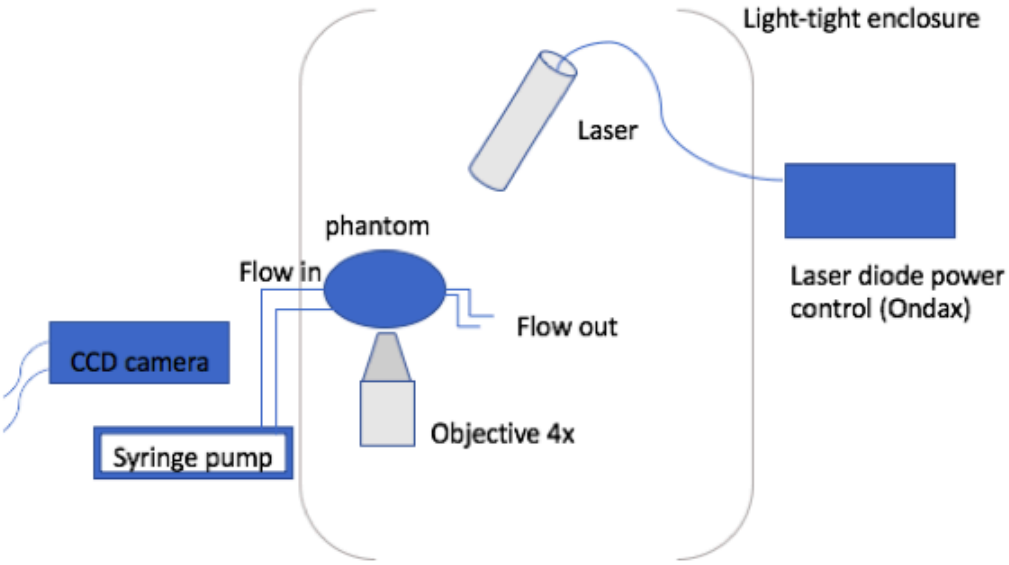

Figure 18: Schematic representation of our flow phantom experiment. The setup is comprised of a few basic elements, including a laser diode, a CCD camera (Retiga 2000R) attached to side port of the inverted microscope, a flow phantom positioned on the microscope stage. The diluted intralipid solution was pumped through the capillary tube via a syringe-based infusion pump.

After adjusting the flow speed of the pump, we used our LSI instrument to acquire a series of raw speckle images from the flow phantom tube that we placed on the microscope stage. Based on preliminary experiments, a camera exposure time of 10 ms was selected as a representative value. For each flow speed, an average of 10 raw speckle images were collected. We used custom-written MATLAB software described in chapter 2 to compute the spatial contrast values

and the decorrelation time (τ_c) of the speckle images at different flow speeds. Briefly, the acquired raw speckle images were converted to speckle contrast images using a 7x7 sliding window algorithm.

Each set of ten speckle contrast images were averaged to obtain one speckle contrast image for each exposure time. In order to identify the flow regions, a percentile analysis was performed via MATLAB. We defined a threshold of 25th percentile for the speckle contrast values. The area with the speckle contrast value of less than the defined threshold was assumed as a flow region. Figure 18 (Right) depicts the raw speckle contrast map and figure 18 (Left) shows ROI region selected by our thresholding method to represent the high flowing tube regions.

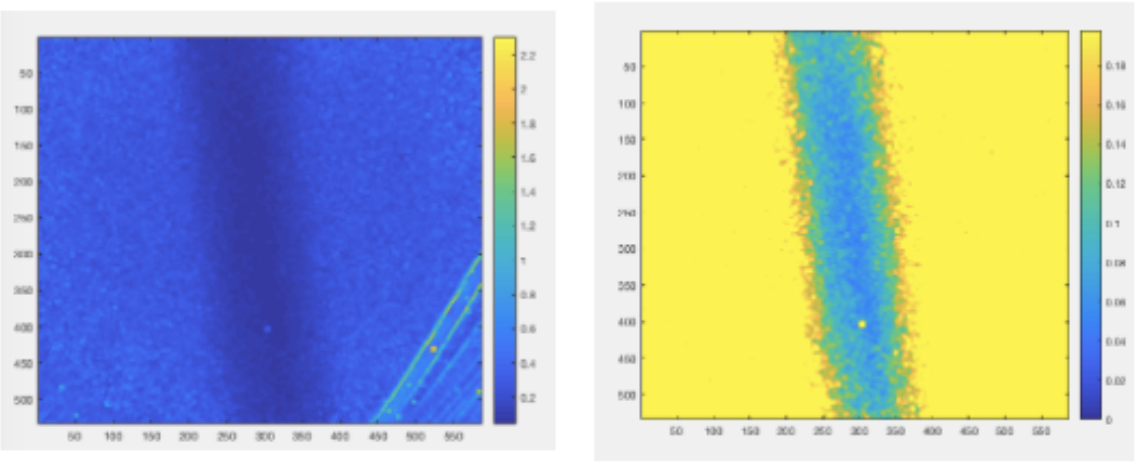

Figure 19: Raw speckle contrast map (Left Figure) acquired from our flow phantom at 10 ms exposure time. Figure on the right shows the ROI region selected by our percentile analysis method to represent the high flowing tube regions.

Results and Discussion:

The flow phantom experiment was performed to study the influence of factors such as camera exposure time and speed of fluid on spatial contrast (K).

Figure (20) presents the results of our *in vitro* experiment, showing that spatial contrast reaches close to zero when there is a significant relative motion, and reaches a maximum value in the case of no motion.

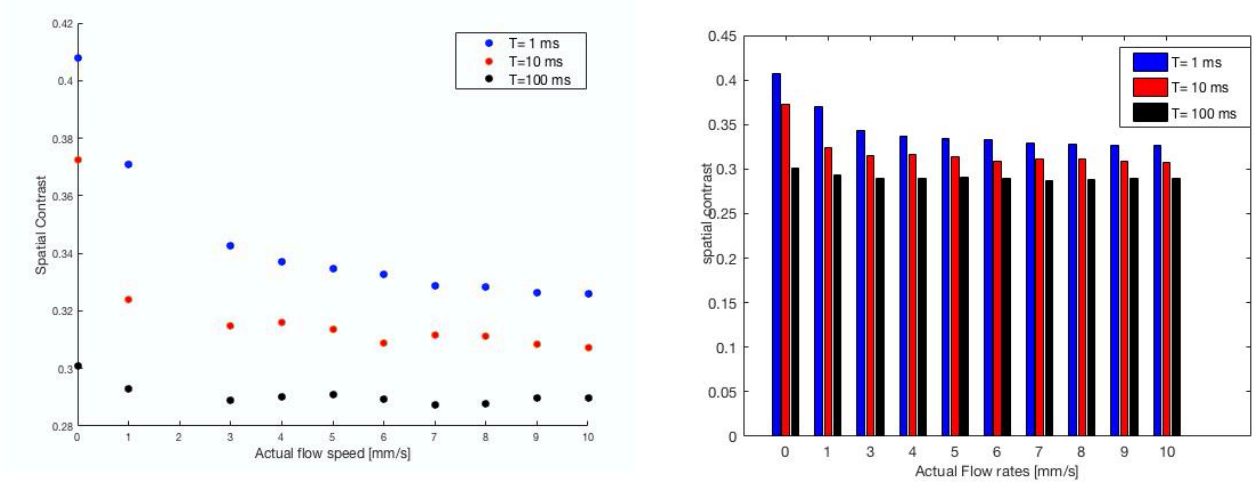

Figure 20: Measured speckle contrast as a function of actual flow speed [mm/s]. Three different exposure times of 1 ms, 10 ms and 100 ms were used. The plots clearly demonstrate the effect of camera exposure time and actual flow speeds on the speckle contrast.

Moreover, our results showed that at a given flow rate, increased exposure time results in a decreased speckle contrast value. For example, by increasing the exposure time from 1 ms to 100 ms, the speckle contrast drops down from 0.41 to 0.3 near 0 mm/s flow speeds. At each flow

speed the speckle contrast has the highest value at 1 ms exposure time and lowest value at 100 ms exposure time.

Our experimental data is in agreement with findings of a study by Parthasarathy et al.[49] who showed that at larger exposure times the sensitivity of relative speckle contrast to blood flow is small near zero speeds, and reaches close to zero at speeds greater than 6 mm/s.

Relationship Between Speckle Flow Index and Actual Flow Rate:

Figure 21 presents the relationship between the computed mean SFI values and the varying flow speeds obtained from our in vitro phantom experiments. Our *in vitro* data suggests that integration of camera exposure time can affect the linear response range of LSI. With 10 ms exposure time, there was a linear relationship between the SFI values and flow speed over 0-10 mm/s. We also observed that by decreasing the exposure time to 1 ms, SFI values were slightly deviated from the linear fit at lower flow speeds (0-5 mm/s). Our experimental data also shows that once we increased the exposure time to 100 ms, SFI values remains unaffected at different flow rates.

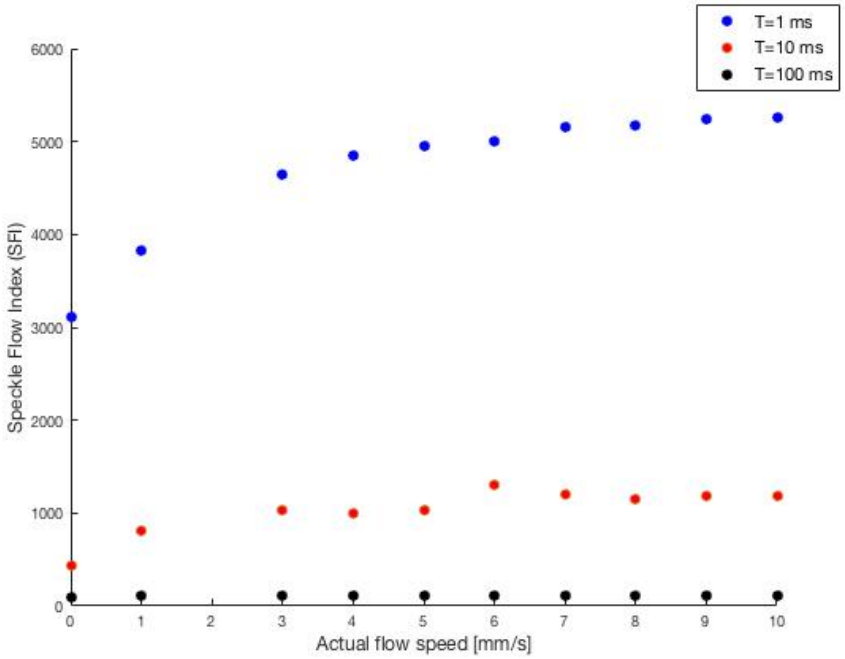

Figure 21: Relationship between the computed mean SFI values and the varying flow speeds obtained from our in vitro phantom experiments.

The data obtained in this experiment enabled us to demonstrate an actual flow rate range over which our LSI instrument has a linear response. Our data is in agreement with a previous study by Choi et al.[48] who demonstrates the effect of camera exposure time on linear response range of SFI values obtained during LSI imaging.

CONCLUSION:

We developed a microvascular imaging system with three different imaging modes: Laser speckle imaging (LSI), Multispectral Imaging/Oxygenation imaging (MSI/O2I) and Fluorescence imaging (FI). Our imaging system enabled us to perform long term monitoring of microvasculature and to obtain non-overlapping details of the biological response to selective

optical injury. We developed image acquisition and processing techniques capable of quantifying blood flow and oxygen saturation levels within the dorsal window chamber. Our LSI technique enabled us to create in vivo maps of relative blood flow providing blood flow information that is valuable in quantifying the dynamic features of angiogenesis. To further asses the microvasculature response to selective optical injury, we integrated multispectral/oxygenation imaging mode to our system. MSI enabled us to create spatial maps of hemoglobin oxygenation based on the light absorption spectra differences between oxygenated and deoxygenated blood.

The validation of the system was conducted through in vitro flow phantom experiments. Collectively, our experimental data strongly suggested that camera exposure time and flow speed are the two important factors that impacts the flow dependent contrast in LSI imaging. We also found that prolonged exposure LSI resulted in an increased structural information on vessels ranging from capillaries to venules. However, use of longer exposure times increases the speckle contrast noise and decreases the imaging contrast K for higher flows. Therefore, long exposure times are only appropriate for visualizing the structure of the vessels rather than quantification of the blood flow within the vessels.

REFERENCES:

1. Lanigan, S. (1997). Videomicroscopy Predicts Outcome in Treatment of Port-Wine Stains. Archives of Dermatology, 133(7), p.921.
2. Frigerio, A., Wright, K., Wooderchak-Donahue, W., Tan, O. T., Margraf, R., Stevenson, D. A., … Bayrak-Toydemir, P. (2015). Genetic V
3. ariants Associated with Port-Wine Stains. PLoS ONE, 10(7), e0133158.
4. Burns, John L. "Vascular anomalies and lymphedema." *Selected Readings Plast Surg* 10 (2006): 1-50.
5. Ashinoff, R. (1991). Capillary Hemangiomas and Treatment with the Flash Lamp-Pumped Pulsed Dye Laser. Archives of Dermatology, 127(2), p.202.
6. Minkis, K., Geronemus, R. and Hale, E. (2009). Port wine stain progression: A potential consequence of delayed and inadequate treatment? Lasers in Surgery and Medicine, 41(6), pp.423-426.
7. Chen, J., Ghasri, P., Aguilar, G., van Drooge, A., Wolkerstorfer, A., Kelly, K. and Heger, M. (2012). An overview of clinical and experimental treatment modalities for port wine stains. Journal of the American Academy of Dermatology, 67(2), pp.289-304.e29.
8. Parish, L. (2011). Andrews' Diseases of the Skin: Clinical Dermatology. JAMA, 306(2).
9. Tanzi, Elizabeth L, Jason R Lupton, and Tina S Alster. "Lasers in dermatology: four decades of progress." *Journal of the American Academy of Dermatology* 49.1 (2003): 1-34.
10. Jasim, Z. and Handley, J. (2007). Treatment of pulsed dye laser–resistant port wine stain birthmarks. Journal of the American Academy of Dermatology, 57(4), pp.677-682.
11. Cole, P., Sonabend, M. and Levy, M. (2007). Laser Treatment of Pediatric Vascular Lesions. Seminars in Plastic Surgery, 21(3), pp.159-166. <http://www.ncbi.nlm.nih.gov/pmc/articles/PMC2884839/>
12. Allemann, I. B., Goldberg, D. J., & S. Karger (Firm). (2011). Basics in dermatological laser applications. Basel: Karger.
13. Anderson, R. and Parrish, J. (1983). Selective photothermolysis: precise microsurgery by selective absorption of pulsed radiation. Science, 220(4596), pp.524-527.

14. Gregory B. Altshuler, Ilya Yaroslavsky. Absorption Characteristics of Tissues as a Basis for the Optimal Wavelength Choice in Photodermatology. Palomar Medical Technologies, Burlington, MA
15. Khandpur, S. and Sharma, V. (2016). Assessment of Efficacy of the 595-nm Pulsed Dye Laser in the Treatment of Facial Port-Wine Stains in Indian Patients. Dermatologic Surgery, 42(6), pp.717-726.
16. Kunishige, J., Goldberg, L. and Friedman, P. (2007). Laser therapy for leg veins. Clinics in Dermatology, 25(5), pp.454-461
17. Jia W., Cheng C., Tan W., Mihm M.C., Stuart Nelson J. (2017) Angiogenesis and Pathogenesis of Port Wine Stain and Infantile Hemangiomas. In: Arbiser J. (eds) Angiogenesis-Based Dermatology. Springer, London
18. G. Aguilar, W. Verkruysse, B. Majaron, L.O. Svaasand, E.J. Lavernia, J.S. Nelson."Measurement of heat flux and heat transfer coefficient during continuous cryogen spray cooling for laser dermatologic surgery." *IEEE Journal on Selected Topics in Quantum Electronics,* 7 (6) (2001), pp. 1013–1021
19. Verkruysse, W., Lucassen, G. and van Gemert, M. (1999). Simulation of color of port wine stain skin and its dependence on skin variables. Lasers in Surgery and Medicine, 25(2), pp.131-139.
20. Phung, T., Oble, D., Jia, W., Benjamin, L., Mihm, M. and Nelson, J. (2008). Can the wound healing response of human skin be modulated after laser treatment and the effects of exposure extended? Implications on the combined use of the pulsed dye laser and a topical angiogenesis inhibitor for treatment of port wine stain birthmarks. Lasers in Surgery and Medicine, 40(1), pp.1-5.
21. Channual, J., Choi, B., Osann, K., Pattanachinda, D., Lotfi, J. and Kelly, K. (2008). Vascular effects of photodynamic and pulsed dye laser therapy protocols. Lasers in Surgery and Medicine, 40(9), pp.644-650.
22. Chen, J., Ghasri, P., Aguilar, G., van Drooge, A., Wolkerstorfer, A., Kelly, K. and Heger, M. (2012). An overview of clinical and experimental treatment modalities for port wine stains. Journal of the American Academy of Dermatology, 67(2), pp.289-304.e29.
23. Jia, W., Sun, V., Tran, N., Choi, B., Liu, S., Mihm, M., Phung, T. and Nelson, J. (2010). Long-term blood vessel removal with combined laser and topical rapamycin antiangiogenic therapy: Implications for effective port wine stain treatment. Lasers in Surgery and Medicine, 42(2), pp.105-112.

24. Velnar, Tomaž, Tracey Bailey, and Vladimir Smrkolj. "The wound healing process: an overview of the cellular and molecular mechanisms." *Journal of International Medical Research* 37.5 (2009): 1528-1542.

25. Anderson, James M. "Biological responses to materials." *Annual review of materials research* 31.1 (2001): 81-110.

26. Nichol, D. and Stuhlmann, H. (2011). EGFL7: a unique angiogenic signaling factor in vascular development and disease. Blood, 119(6), pp.1345-1352

27. Wankhede, Mamta et al. "Spectral Imaging Reveals Microvessel Physiology and Function from Anastomoses to Thromboses." *Journal of Biomedical Optics*15.1 (2010): 011111. *PMC*. Web. 6 Sept. 2017.

28. Johnson, K. and Wilgus, T. (2014). Vascular Endothelial Growth Factor and Angiogenesis in the Regulation of Cutaneous Wound Repair. Advances in Wound Care, 3(10), pp.647-661.

29. Arbiser, J. (2017). Angiogenesis-Based Dermatology. London: Springer.

30. Im, J. and Rajaram, N. (2016). Optical Molecular Imaging and Spectroscopy of Oxygenation and Metabolism in Tumors. IEEE Journal of Selected Topics in Quantum Electronics, 22(3), pp.78-87.

31. Bui, A., Teves, K., Indrawan, E., Jia, W. and Choi, B. (2010). Longitudinal, multimodal functional imaging of microvascular response to photothermal therapy. Optics Letters, 35(19), p.3216.

32. Briers, D., Duncan, D., Hirst, E., Kirkpatrick, S., Larsson, M., Steenbergen, W., Stromberg, T. and Thompson, O. (2013). Laser speckle contrast imaging: theoretical and practical limitations. Journal of Biomedical Optics, 18(6), p.066018.

33. Le, T., Paul, J., Al-Nashash, H., Tan, A., Luft, A., Sheu, F. and Ong, S. (2007). New Insights into Image Processing of Cortical Blood Flow Monitors Using Laser Speckle Imaging. IEEE Transactions on Medical Imaging, 26(6), pp.833-842.

34. Huang, Y., Ringold, T., Nelson, J. and Choi, B. (2008). Noninvasive blood flow imaging for real-time feedback during laser therapy of port wine stain birthmarks. Lasers in Surgery and Medicine, 40(3), pp.167-173.

35. Ramirez-San-Juan J. C., Ramos-Garcia R., Guizar-Iturbide I., Martinez-Niconoff G., and Choi B., "Impact of velocity distribution assumption on simplified laser speckle imaging equation," Opt. Express 16, 3197–3203 (2008).10.1364/OE.16.003197

36. Cheng H. Y. and Duong T. Q., "Simplified laser-speckle-imaging analysis method and its application to retinal blood flow imaging," Opt. Lett. 32, 2188–2190 (2007).10.1364/OL.32.002188

37. White, S., Hingorani, R., Arora, R., Hughes, C., George, S. and Choi, B. (2012). Longitudinal In VivoImaging to Assess Blood Flow and Oxygenation in Implantable Engineered Tissues. Tissue Engineering Part C: Methods, 18(9), pp.697-709.
38. Stern, M.D. In vivo evaluation of microcirculation by coherent light scattering
39. Fercher, A.F. and Briers, J.D. Flow visualization by means of single-exposure speckle photography. Opt Commun 37, 326, 1981.
40. Arimoto, H. (2007). Retinal blood oxygen saturation mapping by multispectral imaging and morphological angiography. IEEE, 60(4), pp.1627-1630.
41. Prahl, S. (2017). Optical Absorption of Hemoglobin. [online] Omlc.org. Available at: http://omlc.org/spectra/hemoglobin/ [Accessed 11 Aug. 2017].
42. Pulseox.info. (2017). What is oxygen saturation?. [online] Available at: http://www.pulseox.info/pulseox/what2.htm [Accessed 11 Aug. 2017].
43. Peter J. Dwyer, Charles A. DiMarzio and R. Rox Anderson. "Mapping Blood Oxygen Saturation using a Multispectral imaging system" SPIE Vol. 2976, pp.270-280, 1997.
44. Guggenheim, J., Basevi, H., Frampton, J., Styles, I. and Dehghani, H. (2013). Multi-modal molecular diffuse optical tomography system for small animal imaging. Measurement Science and Technology, 24(10), p.105405.
45. LUXEON Rebel ES LED, M. (2017). ANSI White (5028K), CoolBase Round 7-Up LED - 1400lm. [online] Luxeon Star LEDs. Available at: http://www.luxeonstar.com/white-5028k-7-led-40mm-round-coolbase-assembly-1400lm [Accessed 11 Aug. 2017].
46. Moy, A., White, S., Indrawan, E., Lotfi, J., Nudelman, M., Costantini, S., Agarwal, N., Jia, W., Kelly, K., Sorg, B. and Choi, B. (2011). Wide-field functional imaging of blood flow and hemoglobin oxygen saturation in the rodent dorsal window chamber. Microvascular Research, 82(3), pp.199-209.
47. Caro, Adam C, F Claire Hankenson, and James O Marx. "Comparison of Thermoregulatory Devices Used during Anesthesia of C57BL/6 Mice and Correlations between Body Temperature and Physiologic Parameters." Journal of the American Association for Laboratory Animal Science : JAALAS 52.5 (2013): 577–583. Print.
48. Uchida, Atsuko & C. Monsma, Paula & Daniel Fenn, J & Brown, Anthony. (2015). Live-cell imaging of neurofilament transport in cultured neurons. Methods in Cell Biology. 10.1016/bs.mcb.2015.07.001.
49. Choi, Bernard et al. "The Role of Laser Speckle Imaging in Port-Wine Stain Research: Recent Advances and Opportunities." IEEE journal of selected topics in quantum electronics:

a publication of the IEEE Lasers and Electro-Optics Society 2016.3 (2016): 6800812. PMC. Web. 11 Aug. 2017.

50. Choi B, Ramirez-San-Juan JC, Lotfi J, Stuart Nelson JJ; Linear response range characterization and in vivo application of laser speckle imaging of blood flow dynamics. J. Biomed. Opt. 0001;11(4):041129-041129-7

51. Parthasarathy, Ashwin & Gyu Shin, Weon & Zhang, Xiaojing & Dunn, Andrew. (2007). Laser Speckle Contrast Imaging of flow in a microfluidic device - art. no. 644604. Proceedings of SPIE - The International Society for Optical Engineering.10.1117/12.700572.

APPENDIX:

Microscope Operating Procedure

Initial preparation

- Mount Retiga 2000R camera on Microscope system
- Connect Retiga to computer:
  Plug one end of the Firewire cable into one of the camera's Firewire sockets (either socket is fine). Plug the other end of the cable into a Firewire port of your computer.
- Turn the camera on by pushing the power switch to "I" position.

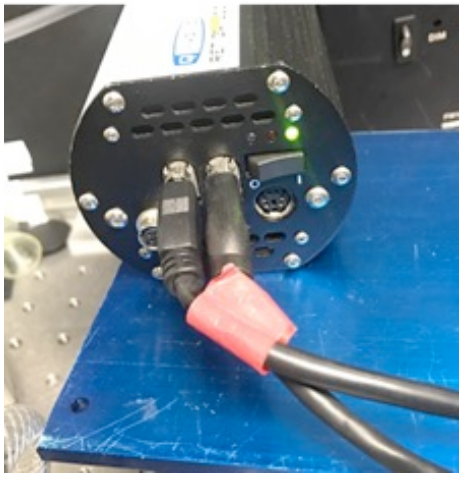

- Turn the heater on

- Open MATLAB 2015

Multispectral Imaging

Filter Wheel preparation

- Load the Filter Wheel with filters by first removing the filter wheel cover, which is held in place with a single thumbscrew.

- Insert the filters into the desired locations. (Note that you need to input the corresponding wavelength for each filter position in the FW102C software, i.e. Change Filter 1 to WL_550nm Pos: 1)

- Secure the filters with retaining rings and put the cover back in place
- Connect the power cord from the AC adapter into the DC input jack on the unit
- Connect Filter wheel to computer via RS 232 serial port using a serial cable

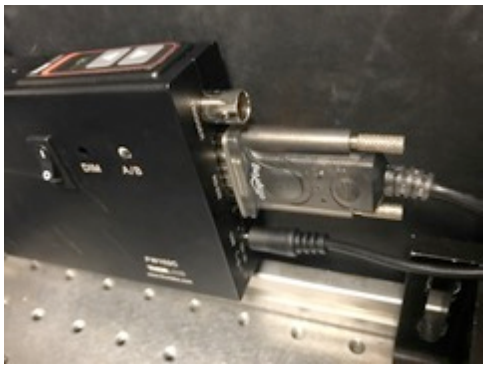

- Turn on the filter wheel using the key switch located on the side

- Open FW102C software. Press Connect. Select the device (COM6).

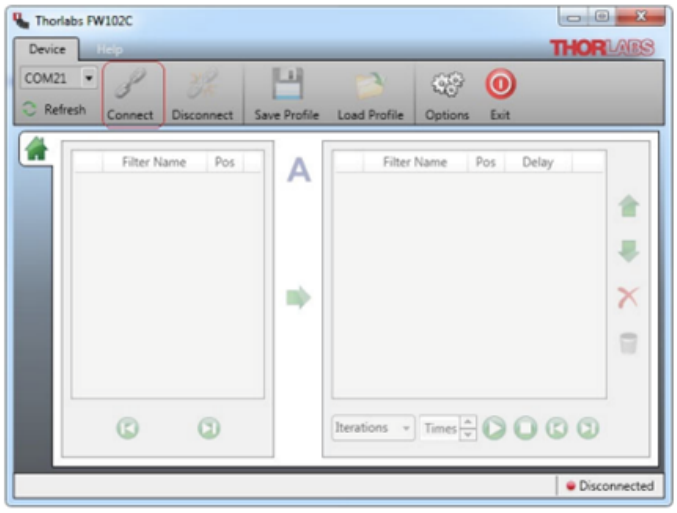

Set up iteration mode on FW102C (OPTIONAL)

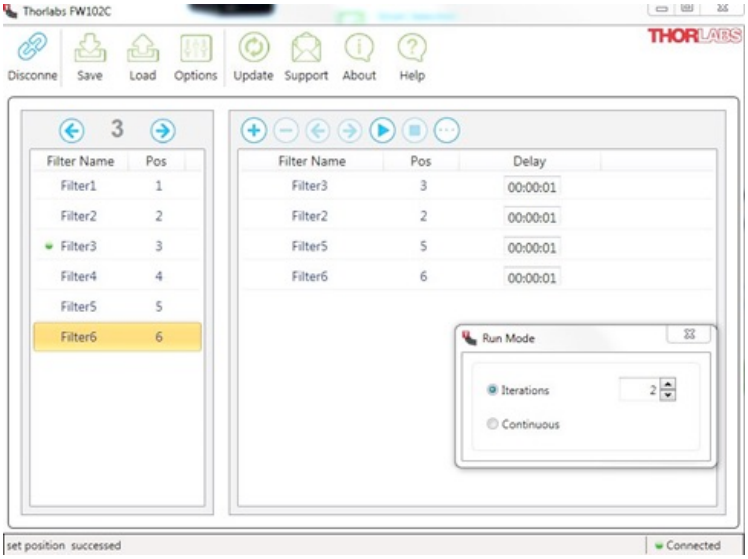

- Set up the filter location sequence and delay time in the box on the right
- Select Iteration in the drop-down box
- Specify the number of times the sequence will run

- To acquire image:
    - Turn on power supply and voltmeter (set to 5V) using switch

    - Run ImageAcquisition_MSI.m code: (C:\Users\Ben\Bita\ImageAcquisition_MSI.m)

- Enter the Imaging session number in the prompt, then click OK
- On the next prompt window select the corresponding wavelengths to the loaded filters, then click OK
- Check the extinction coefficient values on the next prompt: (Note: you can edit the values), then click OK
- Change the FilterWheel position to “Blank” filter position
- The image preview will appear

- To select ROI:
  - Move translational stage.
- To focus ROI:
  - Adjust coarse knob

- On FW102C, press the filter position to adjust the filter locations.

  Note: you can do this manually by pushing the ▲ / ▼ arrow buttons on the top of the unit to adjust the filter location)
  Note: If Iteration mode is set -> click Run on FW102C to initiate Filter Wheel Sequence

- Press OK with each prompt to save the raw image for each filter
- Turn off power supply and light switch.

To Process MSI images:

1. Run MSI_Function_Bita.m code:
   (C:\Users\Ben\Bita\ MSI_Function_Bita.m)

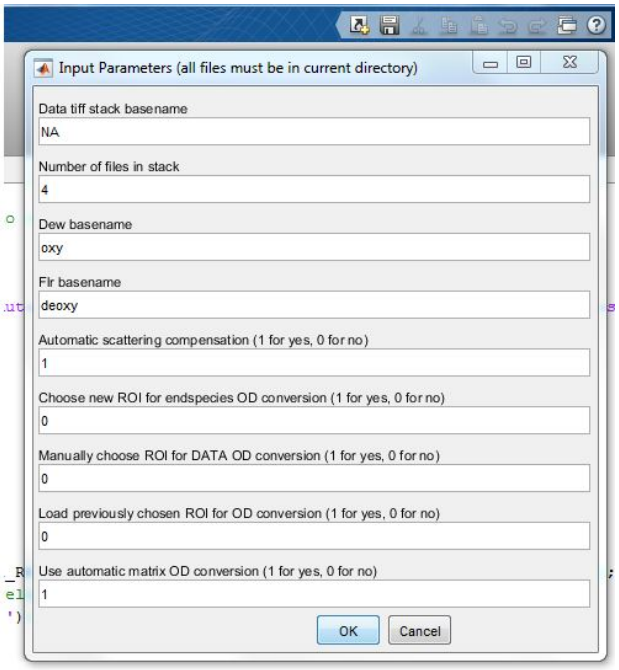

2. On the prompt, check the number of files (i.e., total number of images acquired in the 'acquire image' section), the rest of the parameters are predefined. Click OK
3. The next window lets you select a rectangle in the figure window using the mouse. Draw a rectangle and double click to proceed.
4. Input # 5 on the next prompt asking for grid size
5. Repeat step 3
6. Code will process the image and saves the results in a folder corresponding to the session number.
7. End

For Laser Speckle Imaging (LSI)

- Make sure Ondax 785nm, 100mW is connected to power source and key switch is turned on.

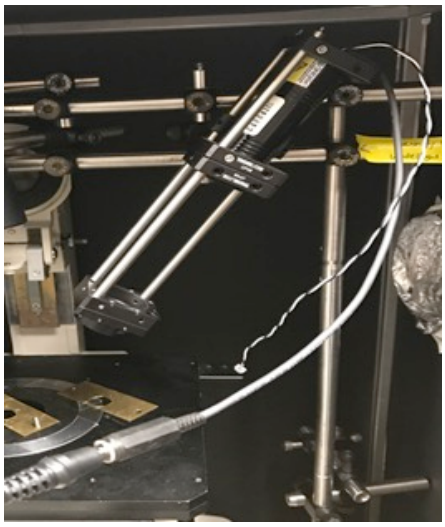

- Turn on laser key switch; wait for laser to turn on.

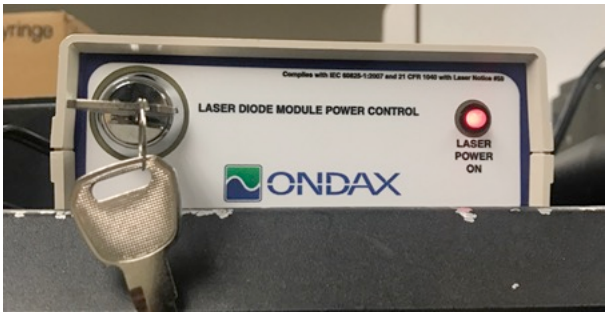

To Acquire Image:

a. Run ImageAcquisition_Bita.m code: (C:\Users\Ben\Bita\ImageAcquisition_Bita.m)
b. Select the exposure time (10 or 1000ms) on the prompt window:
c. Adjust intensity using ND Filters:
    i. For 10 ms exposure time use ND: 1
    ii. For 1000 ms exposure time use ND: 4
d. To select ROI:
    i. Move translational stage.
e. To focus ROI:
    i. Adjust coarse knob.

f. Click OK to save the images (The code will acquire 10 raw images and automatically saves them in the folders corresponding to the selected exposure time)

g. Repeat Steps (a-f) for each exposure time. (make sure to change the ND filters for the next exposure time)

h. Switch laser key off.
i. Remove Firewire Cable.

To Process Image:

1. Run calculateSFI_TIFF_Bita.m
2. (C:\Users\Ben\Bita\calculateSFI_TIFF_Bita.m)
3. On the 'Process which type of image' prompt, select NOT Raw Bayer Images
4. Select Spatial Correlation on the next prompt
5. Input 7 for sliding window size (n x n)
6. Save SFI maps
7. End

For Fluorescence imaging (FI)

To Acquire Image:

- Mount QUANTEM camera on to the Microscope system
- Connect QUANTEM to computer using a USB cable
- Insert the filter cube with appropriate filters into the filter cube holder (Note: The choice of a specific filter block will depend on the fluorescent probe(s) being used in the imaging application)
- Cover the microscope eyepiece during imaging
- Turn on the BWF Laser key switch.
- Open Micro-Manager software on the computer
- Click LIVE to preview
- Set the desired exposure time on the camera setting

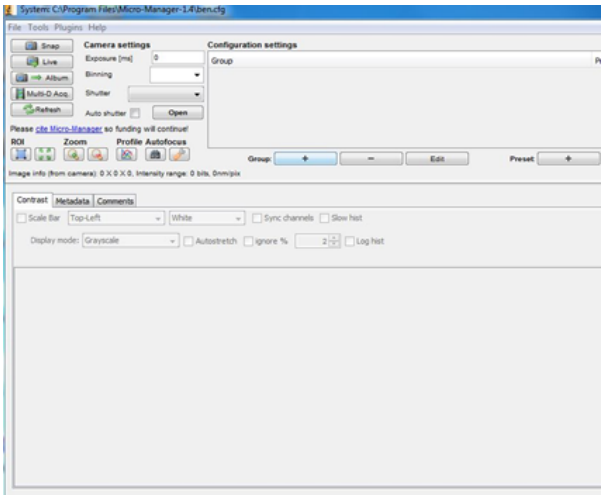

- To select ROI:
    - Move translational stage.
- To focus ROI:
    - Adjust coarse knob

- Click on Multi-D Acquisition Tab. Note that here you can set the time points and choose the directory to save your images.